Applied Clay Science 276 (2025) 107917

Contents lists available at ScienceDirect

Applied Clay Science

journal homepage: www.elsevier.com/locate/clay

Research Paper

Evaluation of the potential toxicity of respirable halloysite elongate mineral particles: Insights from the Fibre Potential Toxicity Index (FPTI) model

Alessandro F. Gualtieri [a,b], Laurie Glossop [c], Daniele Malferrari [a,b,*], Elena Castellini [a], Magdalena Lassinantti Gualtieri [d], Miriam Hanuskova [d], Luca Nodari [e], Jordan Ogor [f], Riccardo Fantini [a]

[a] Department of Chemical and Geological Sciences, University of Modena and Reggio Emilia, Via G. Campi 103, I-41125 Modena, Italy
[b] Inter-Departmental Research and Innovation Centre on Construction and Environmental Services of the University of Modena and Reggio Emilia, Via P. Vivarelli 10, I-41125 Modena, Italy
[c] Glossop Consultancy, 1 Cumnock Place, Duncraig, WA 6023, Australia
[d] Engineering Department "Enzo Ferrari", University of Modena and Reggio Emilia, Via P. Vivarelli 10, I-41125 Modena, Italy
[e] CNR-ICMATE, Corso Stati Uniti 4, I-35127 Padova, Italy
[f] COHLABS, Suite 2, 92 Cleveland Street, Greenslopes, Coorparoo, QLD 4151, Australia

ARTICLE INFO

Keywords:
Airborne particulate
Elongate mineral particle
Halloysite
Nanotubes
Fibre potential toxicity index

ABSTRACT

Halloysite is a member of the kaolin group, with an ideal chemical composition of $Al_2(OH)_4Si_2O_5{\cdot}2H_2O$, displaying wide and diverse industrial application spanning from traditional ceramics to drug delivery. Halloysite often occurs as elongate mineral particles (EMPs) with nanometer-size tubular, cylindrical or fibrous shape. Despite these features and its extensive use, the International Agency for Research on Cancer (IARC) has not yet evaluated halloysite for its potential carcinogenicity. Existing literature only focused on its toxicity following oral administration mostly in a pharmaceutical contexts, but findings remain inconclusive.

In this study, a commercially available halloysite from Matauri Bay (North Island, New Zealand) was investigated to provide further insight into potential occupational exposure to airborne nano-particles in the ceramic industry. A comprehensive characterization of the sample was performed using XRPD, TGA-DTA, XRF-WDS, BET, particle size distribution, SEM, TEM, Mössbauer and UV–Vis spectroscopies. This multi-technique approach permitted to determine its toxicity potential through the Fibre Potential Toxicity Index (FPTI) model, which had already proven robust in evaluating the hazardousness of respirable mineral fibres. Results indicated that the sample contains approximately 90 wt% halloysite, with minor quartz and cristobalite. Halloysite nanotubes are respirable but not "regulated fibres" with a FPTI value of 1.92(0.10), comparable to that of non-carcinogenic mineral fibres suggesting, with caution, that halloysite is a nanomaterial with low toxicity. Although the study focused on samples from a specific locality, the results should be considered applicable to halloysite samples from any quarry; nevertheless, it should be noted that halloysite from this deposit contains respirable quartz and cristobalite which are a IARC *Group 1* known human carcinogens.

1. Introduction

Halloysite is a layer silicate that occurs in both weathered rocks and sedimentary deposits, formed by the alteration of a wide variety of rock types (Joussein et al., 2005). Halloysite shares the same ideal chemical composition as kaolinite, except for the interlayer content of water. Moreover, kaolinite exhibits a flat layered crystal structure, while halloysite a rolled structure with a hollow core. At a basic level, both minerals are composed of Si-centred tetrahedral sheets arranged in a pseudo-hexagonal network joined to Al-centred dioctahedral sheets in units with a 1:1 ratio. Halloysite, containing water in the interlayer space, results in the ideal formula $Al_2Si_2O_5(OH)_4{\cdot}2H_2O$. AIPEA Nomenclature Committee (Joussein et al., 2005) approved the terms halloysite-(10 Å) ($n = 2$; $d_{001} \approx 10$ Å) for the hydrated mineral and halloysite-(7 Å) ($n = 0$; $d_{001} \approx 7$ Å) for the dehydrated form (Bailey, 1980). The analysis of halloysite diffraction patterns, biased by the

* Corresponding author at: Department of Chemical and Geological Sciences, University of Modena and Reggio Emilia, Via G. Campi 103, I-41125 Modena, Italy.
E-mail address: daniele.malferrari@unimore.it (D. Malferrari).

https://doi.org/10.1016/j.clay.2025.107917
Received 17 February 2025; Received in revised form 9 June 2025; Accepted 18 June 2025
Available online 3 July 2025

presence of extensive planar defectivity, revealed a triclinic to monoclinic symmetry with the most common monoclinic space group *Cc* (Bailey, 1980). The mean unit cell parameters calculated from the literature data reported in Table 2, page 390 of Joussein et al. (2005) with standard deviations are: $a = 5.138(4)$Å; $b = 8.907(15)$Å; $c = 14.65(18)$Å; $\alpha = 90.53(84)^\circ$; $\beta = 98.88(5.6)^\circ$; $\gamma = 90^\circ$.

Deviations from the ideal chemical composition of halloysite are observed, as isomorphous substitution of Fe^{III} for Al^{III} are possible in the octahedral sheet (see for example, Muller and Calas, 1989; Hart et al., 2002). Watanabe et al. (1969) and Soma et al. (1992) also assumed some irregular replacement of Si^{IV} by Al^{III} in the tetrahedral sheet for halloysite samples from Nagasaki (Japan) and New Zealand, respectively. Titanium, commonly associated to halloysite- and kaolinite-rich materials, is usually attributed to impurities of oxides, such as anatase (TiO_2) (see for example, Schroeder and Shiflet, 2000).

Halloysite predominantly exhibits a tabular morphology, although cylindrical and fibrous shapes have also been documented (Joussein et al., 2005). Particles with these shapes generally have a length to width ratio (aspect ratio) greater than 3, qualifying them as *elongate mineral particles* (EMPs) (Gunter, 2018). The variability of the shape of halloysite is due to many factors including crystal structure, degree of alteration/dehydration, and chemistry (Joussein et al., 2005). Regarding chemistry, when the degree of isomorphous substitution of Fe^{III} for Al^{III} in the octahedral sheet increases, the layer curvature decreases and the shape is more platy-lamellar like kaolinite. If the substitution is non-stoichiometric, Soma et al. (1992) showed that creation of vacancies in the octahedral sheet might increase the layer curvature.

Halloysite clay, mainly due to the high alumina content, plasticity, and whiteness has long been used by ceramic industries for the production of traditional ceramics (*e.g.*, ceramic tiles and tableware: Wilson, 2004), advanced or high-tech ceramics and ceramic composites like coatings and membranes (Lampropoulou and Papoulis, 2021).

Halloysite nanotubes, nanometric tubular particles that generally have a hollow core, can function as time-release capsules that gradually dissolve over time. They can be filled with various additives for use in paints, sealants, lubricants, herbicides, pest repellents, household, food, personal care products and cosmetics; additionally, they can serve as molecular sieves in a wide range of applications, including separation of liquids and gaseous mixtures, water purification in refining industries, and also in the remediation of acid mine drainage (Joussein et al., 2005; Fahimizadeh et al., 2024). Halloysite, both natural and synthetic, is also used for the fabrication of biomaterials and drug delivery vehicles (Lazzara et al., 2018; Zhang et al., 2025), as well as in cell supporting scaffolds for tissue engineering (Naumenko and Fakhrullin, 2017), antimicrobial coatings (Wei et al., 2014), and as nanocarrier for intracellular delivery of drugs and enzymes (see for example, Massaro et al., 2018a).

Given the increasing massive use of natural and synthetic halloysite products, at one point the question arose as to whether halloysite and, especially, halloysite nanotubes (Hal here after) and EMPs might pose a hazard to human health. Notably, halloysite has never been evaluated by the International Agency for Research on cancer (IARC) as a potential carcinogenic agent. Existing literature focused on assessing the toxicological effects of Hal through oral administration, largely due to its extensive use in pharmaceutical applications. To the best of the authors' knowledge, a survey of the existing literature data allows the results to be grouped into three distinct but interconnected groups: (a) those indicating that Hal are non-toxic; (b) those showing evidences of toxicity of Hal only at high/very high doses; (c) those showing evidences of toxicity of Hal.

The first cluster of results indicates that halloysite, with special attention to Hal, should be considered non-toxic (Vergaro et al., 2010; Chiriacò et al., 2014; Sánchez-Fernández et al., 2014; Liu et al., 2015; Maisanaba et al., 2015; Jaurand, 2016; Brandelli, 2018; Massaro et al., 2018b; Rozhina et al., 2021; Biddeci et al., 2023). Fakhrullina et al. (2015) used the nematode microworm *Caenorhabditis Elegans* as a model organism and found that halloysite is localised exclusively in the alimentary system and does not induce severe toxic effects. Long et al. (2018) assessed that Hal are relatively non-cytotoxic for human umbilical vein endothelial cells (HUVECs), human breast adenocarcinoma (MCF-7) and for zebrafish embryos *in vivo*. Santos et al. (2019) claimed that Hal are safe and biocompatible low-toxicity nanomaterials to be used for drug encapsulation for numerous clinical applications. Barfod et al. (2020) found that Hal do not induce cytotoxicity *in vitro*, but the functionalization of their surface by etching led to increased pulmonary inflammation and acute phase response of Hal following pulmonary dosing in mice, suggesting that precautions should be taken with modifications that increase the specific surface area of nanoparticles. Wu et al. (2020) compared the toxicity of Hal and multi-walled carbon nanotubes (MWCNTs) to human umbilical vein endothelial cells (HUVECs) *in vitro* and blood vessels of mice *in vivo*. These authors concluded that Hal are probably safer nano-carriers compared with MWCNTs. Biddeci et al. (2023) summarized the results of *in vitro* effects of Hal on HeLa (human cervical cancer) and Raw 264.7 (murine macrophage) cells by MTS assay with different concentrations, showing that the viability was almost 80 % for the highest concentration in HeLa cells and close to 100 % in Raw 264.7 following a 24 h incubation. Even after prolonged treatments (48 and 72 h), cell viability remained high for both cell lines.

The second group of literature data shows evidences of toxicity of Hal only at high/very high doses (*ca.* 200–1000 μg/mL). The toxicity of Hal at different concentrations was further evaluated against human peripheral lymphocytes by mitotic index assay, which revealed the inhibition of the lymphocyte's proliferation only at the highest concentration (1000 μg/mL) (Ahmed et al., 2015). Zhao et al. (2019) investigated the toxicity of Hal with *in vitro* assays on mBMSCs and UMR-106. Massive cells death, including mBMSCs and UMR-106, was observed at the higher Hal concentration of 200 μg/mL. *In vivo*, the results of the *Caenorhabditis Elegans* model showed that Hal had not a long-term toxicity, inducing a slight upregulation of the oxidation-related genes but not causing a significant increase in ROS production. The *Caenorhabditis Elegans* experiments suggested that Hal, below the concentration of 1 mg/mL, had no obvious toxicity (Fakhrullina et al., 2015). Cytotoxic and genotoxic effects of Hal from various deposits in the world was evaluated through MTT and CBMN assay on mammalian cell cultures (Lazzara et al., 2023). The results showed that at low doses and shorter times, Hal exhibited a low level of cytotoxicity, while moderate levels of toxicity were observed at high concentrations and for long periods of exposure.

The third group of literature data reports evidence of toxicity of halloysite which may therefore suffer from some toxicity issues once it interacts with tissue and cells, for drug delivery and bio-imaging applications (Leporatti et al., 2020). Tarasova et al. (2019) showed that coating of Hal by polyelectrolytes such as poly(ethylenimine), poly (diallyldimethylammonium chloride) and poly(allylamine) hydrochloride increased the colloidal stability of Hal in aqueous dispersions; interaction of high concentrations of stabilized Hal with lung carcinoma cells culture promoted changes in the morphology of cell nuclei, whereas no changes were observed in the case of pristine Hal. Wang et al. (2018) assessed the hepatic toxicity of the purified Hal in mice *via* oral route. Oral administration of Hal inhibited the growth of the mice at the middle (50 mg/kg BW) and high (300 mg/kg BW) doses. In addition, oral administration of Hal at the high dose caused Al accumulation in the liver but had no marked effect on the Si content in the organ. The Al accumulation caused significant oxidative stress in the liver, which induced hepatic dysfunction and histopathologic changes. Rong et al. (2019) evaluated the toxicity of inhaled Hal and found that they can cause sub-chronic toxicity in mice. These authors reported that Hal (with unspecified kaolinite content) induce autophagy blockade leading to the accumulation of sequestosome-1 (p62), which in turn contributes to excessive apoptosis, inflammatory response, and oxidative stress. Luo et al. (2020) measured the cytotoxicity of synthetic commercial grade

Hal against CT26WT (murine colorectal cancer) cells and the results showed that after 24 h of treatment at 150 μg/mL, it is possible to observe a 25 % decrease in cell's viability. This value continues to decrease with the increasing concentration of Hal. Sawicka et al. (2021) investigated the short- (24 or 72 h) and medium-term (7 d) cytotoxic effects of Hal on human alveolar carcinoma epithelial cells (A549) and human bronchial epithelial cells (BEAS-2B). These authors showed that cytotoxicity of Hal is dependent on dose, cell model and time of exposure, suggesting a potential chronic toxicity. Morphological changes observed in cells confirmed the cytotoxic effect of Hal even at low doses, calling for further studies using different cell models to more comprehensively assess its toxicological profile.

The potential toxicity of halloysite *via* inhalation remains an open and insufficiently addressed issue. The early study of Stanton et al. (1981) showed that pleural dose to 40 mg of Hal in hardened gelatin implanted on to the pleural surface resulted in formation of pleural sarcomas in 9 of 53 rats (17 %) 2 y post-exposure as compared to 3 of 488 sham-treated controls (0.6 %). Koivisto et al. (2018) assessed the potential inhalation exposure to Hal in an industrial research laboratory; given the very limited toxicological data on Hal, the authors recommend avoiding inhalation exposure as a precautionary measure.

Considering the elongated shape of the halloysite particles and mindful of the experience with asbestos, the present work aims to contribute to the ongoing discussion by calculating the toxicity potential of respirable halloysite EMPs. To this aim, the Fibre Potential Toxicity Index (FPTI) model (Gualtieri, 2018, 2021), which has been used in the past to analyse various mineral fibres (*e.g.*, fibrous glaucophane: Di Giuseppe et al., 2019; chrysotile: Di Giuseppe et al., 2021a), was applied. The FPTI model considers all the physical/crystal-chemical/morphological parameters of a respirable (exposure by inhalation and not digestion) mineral fibre that induce biological mechanisms responsible for adverse effects and allows the toxicity/pathogenicity potential of the fibre to be determined. The fibre parameters considered in the model are: morphometric (the fibre length, width, crystal curvature, crystal habit, density, hydrophobic character of the surface, specific surface area); chemical (total iron content, ferrous iron, surface ferrous iron/iron nuclearity, content of metals other than iron); biodurability-related (dissolution rate, velocity of iron release, velocity of silica dissolution, velocity of release of metals); surface activity (zeta potential, fibres' aggregation, cation exchange).

The fibre parameters induce specific adverse effects that tied to *in vivo* pathological processes attributed to key characteristics of carcinogens (Gualtieri, 2021); the 10 KC parameters (Smith et al., 2016) used by IARC to evaluate the strength of the mechanistic evidence for an agent are:

1. Is electrophilic or can be metabolically activated?
2. Is genotoxic?
3. Alters DNA repair or causes genomic instability?
4. Induces epigenetic alterations?
5. Induces oxidative stress?
6. Induces chronic inflammation?
7. Is immunosuppressive?
8. Modulates receptor-mediated effects?
9. Causes immortalization?
10. Alters cell proliferation, cell death or nutrient supply?

IARC reviewed all information and data of human carcinogenesis mechanisms and found that *Group 1* agents (like asbestos minerals) show one or more of the 10 KCs (Smith et al., 2016).

The sample investigated in this study is a processed commercial natural sample of halloysite from Matauri Bay (North Island, New Zealand) widely used in the ceramic industry for glazes. This widespread use and the availability of published data on materials from the same area are the reason for choosing this specific deposit; nevertheless, the results obtained and the application of the model should be considered valid for any halloysite sample regardless of origin. This study aligns with the current need to better understand and classify the potential occupational exposure to airborne nano-particles in the ceramic industry (Bessa et al., 2020).

2. Materials and methods

2.1. Material

As mentioned above and according to Christie et al. (2000), Keeling et al. (2015), Wilson and Keeling (2016) and references therein, the material investigated is a "processed product" that has undergone a number of processing steps prior to market release. Specifically, the raw clay is first blended from stockpiles and wet ground in a pan mill. Successive autogenous grinding, hydrocyclones, settling boxes and centrifuges are used to reduce levels of fine-grained silica. The beneficiated clay is thickened, dewatered by filter pressing and the filtercake is either extruded at 37 wt% moisture or shredded and dried to produce granules and powders with <5 wt% moisture content. The sample is marketed in Australia with code BA 139 kaolin. No further preparation was performed on the material other than those necessary for the experimental measurements described below.

2.2. Analytical methods and experimental conditions

A representative batch of the halloysite sample was gently hand-ground using an agate mortar and mixed with 10 wt% of corundum (α-Al_2O_3) NIST 676a as an internal standard. X-ray powder diffraction (XRPD) data collection was performed using a θ–θ Bragg-Brentano Panalytical'XPert Pro Diffractometer equipped with a Cu Kα radiation (λ = 1.5418 Å) tube operating at 40 kV and 30 mA and a real time multiple strip (RTMS) detector. The measurement was performed in the 3–85°2θ interval, with: 0.02 rad Soller slit, 10 mm mask, ½° divergence slit and ½° anti-scatter slit on the incident beam and 5.0 mm anti-scatter slit on the diffracted beam. The counting time was of 85 s each 0.0167°2θ step.

Quantitative phase analysis (QPA) was performed using the Rietveld methods as implemented in PROFEX version 5.3.0 software (Döbelin and Kleeberg, 2015). The disordered model of kaolinite present in PROFEX database was employed to reproduce the signal of halloysite while the structure of quartz (Kihara, 1990) and cristobalite (Downs and Palmer, 1994) were taken from the American Mineralogist Crystal Structure Database.

Thermogravimetric (TGA) and thermodifferential (DTA) analyses were conducted using a Seiko SSC 5200 thermal analyser on about 15 mg of finely ground material. The heating rate was 10 °C min^{-1} from 25 to 1050 °C. Measurements were carried out in air and data (TGA and DTA signals) acquired every 0.5 s. α-alumina powder was used as reference for DTA.

X-ray fluorescence (XRF) analyses were carried out using the Malvern Panalytical Zetium (Eindhoven, Netherlands) sequential wavelength dispersive spectrometer, operating under vacuum conditions, equipped with 3 kW Rh tube and 5 analyser crystals (LiF220, LiF200, Ge, PE, PX1) operating alternately depending on the element to be analysed. Measurements were performed on a tablet of pressed powder (15 t for 3 min) on a boric acid support. The tablet consisted of 2.7 g of halloysite clay, previously calcined at 980 °C for 3 h, mixed with 0.3 g of organic adhesive. Analyses are considered accurate within 2–5 wt% for major elements (Na, Mg, Al, Si, P, K, Ca, Ti, Mn, Fe), and better than 10 wt% for trace elements (F, S, Cl, Sc, V, Cr, Co, Ni, Cu, Zn, Ga, As, Rb, Sr, Mo, Cd, Sn, Sb, Cs, Ba, Pb, La, Ce, Nd, Th and U).

The BET specific surface area (SSA) was measured using a Gemini V instrument (Micromeritics) and nitrogen as probe gas and used for the calculation of FPTI score (Section 3). About 500 mg of sample was mounted in the sample holder and conditioned at 105 °C prior to measurement. The precise weight of the sample was consequently

determined using an analytical balance.

The particle size distribution was measured by laser diffraction and the Mie theory using a Mastersizer 2000 (Malvern Instruments Ltd.) equipped with a wet dispersion unit (Hydro 2000s). The sample was prepared as follows: about 300 mg of sample was dispersed in 50 mL of an aqueous solution of sodium tripolyphospate (TPF, 0.3 wt%). The dispersion was left overnight under magnetic stirring and subsequently used for *in situ* tests during which the power of the ultrasonic equipment implemented in the dispersion unit was varied. The sample was inserted in the wet dispersion unit of the instrument until ideal obscuration *(i.e.*, 10–20 %) was reached; an aqueous TPF solution (0.3 wt%) was used as carrier fluid. The real and imaginary part of the refraction index was iteratively determined (1.69 and 0, respectively) by manual tuning until a residual <1 % was obtained (indicating satisfactory fit between the calculated and observed data). The particle size distribution was followed as a function of a large number of consecutive measurements (>100) during which the ultrasonication power was gradually increased from 0 to 50 %. Within the time frame of the experiment, 50 % ultrasonic power resulted in highly stable and reproducible results.

The scanning electron microscope (SEM) experiments were conducted using a JSM-6010PLUS/LA (JEOL, Hillsboro, OR, USA) equipped with an energy-dispersive X-ray (EDX) microanalysis system (Oxford INCA-350) and field emission gun scanning electron microscope FEI Nova NanoSEM 450 FEG-SEM. All the samples were mounted on an Al stub and coated with Au using a Balzers CED-010 carbon coater (10 nm thick).

The transmission electron microscopy (TEM) data were collected using HITACHI model HT7700. Operating acceleration voltage is 100 kV. The EDX detector is a Thermofisher device and the EDX software is Noran System (NSS7). For the determination of the size and width of the halloysite fibres, the operating magnification was 10,000×. A graticule on one grid opening was observed and the structures visible in that graticule were documented. Further TEM analyses to elucidate the nature of iron in the sample were performed with a Thermo Fisher Scientific Talos F200S G2 FEG-TEM instrument equipped with a CETA 16 M CMOS camera, STEM detectors, in HAADF (high-angle-annular-dark-field scanning transmission electron microscopy), ADF, ABF and BF-STEM (bright field scanning transmission electron microscopy) modes, and EELS with Gatan Enfinium SE/976 detector. Few milligrams of the specimen were suspended in a vial with 0.1 % Aerosol OT surfactant in distilled water, and then sampled with a TEM copper grid. Images were collected at 200 keV.

Room temperature Mössbauer spectroscopy (MS) was performed using a constant acceleration spectrometer equipped with a room-temperature Rh matrix ^{57}Co source of nominal strength 1850 MBq. The spectra were collected by dispersing ≈1000 mg of ground powder in petroleum jelly placed in a 38 mm sample holder. An LND, Inc. 4012cylindrical proportional counter was used. The obtained spectra were fitted to Lorentzian line shapes using a minimum number of doublets. The obtained hyperfine parameters isomer shift (δ), quadrupole splitting (Δ) and half line-width at half maximum (Γ_+) are expressed in mm/s, while the relative areas (A) are in %. The velocity was calibrated against an α-Fe foil, and δ is quoted relative to metallic iron at room temperature.

2.3. Determination of the toxicity potential of the halloysite EMPs

The FPTI model (Gualtieri, 2018, 2021) was used to calculate the toxicity potential of the halloysite EMPs present in the sample. For each parameter of the model (mean fibre length and diameter, crystal habit and curvature, density, hydrophobic character, specific surface area, iron content, content of ferrous iron, surface iron and its nuclearity, content of metals other than iron, fibre dissolution rate, rate of iron dissolution/release, rate of silica dissolution/release, rate of release of metals from the fibre, surface reactivity, zeta potential, aggregation state of the fibres in suspension), a score is assigned based on its measured value, its susceptibility to induce adverse effects and its weight in the model. The $FPTI_i$ is then calculated from the equation (Gualtieri, 2018):

$$FPTI_i = \sum_{i=1}^{n} w_1 w_2 T_i$$

where $w_1 = 1/H$ weight of the parameter according to its hierarchy H; $w_2 = 1/U$ weight of the parameter according to the uncertainty U of its determination; T_i = class value of the parameter i^{th} of the model. All the details of the model are explained in Gualtieri et al. (2021) and the WebFPTI manual freely available at https://fibers-fpti.unimore.it/FPTI/ that includes the calculation of the errors associated with each parameter.

In addition to the TEM and Mössbauer data, following the protocol described in Gualtieri et al. (2024), the indication on the iron nuclearity (parameter (1,10) of the FPTI model) was confirmed by the shape of the UV–Vis spectrum. A UV–VIS–NIR (JASCO V-570) spectrophotometer equipped with an integrating sphere attachment (JASCO model ISN-470) was used with $BaSO_4$ as reference. The bandwidth was set at 10 nm, and the scan speed was 400 nm/min. For the measurement, 100 mg of sample, ground as homogeneously as possible, was used. The spectrum was normalized and the derived Multivariate Curve Resolution (MCR) model was applied to predict the values of the components C1, C2, C3 and C4 for the sample (Gualtieri et al., 2024). High values of C1 indicate isolated Fe^{III}, high values of C2 indicate cluster Fe^{II} and Fe^{III}, high values of C3 indicate Fe^{III} cluster, and high values of C4 indicate isolated Fe^{II}. Intermediate values of both C1 and C3 are also possible and these are interpreted as iron with low nuclearity. The assignment of the value of the nuclearity-related toxicity parameter (1.10) is then (Gualtieri et al., 2024):

- high values of the component C1 (isolated Fe^{III}) or C4 (isolated Fe^{II}) → iron nuclearity = 1 → index value = 0.07 (high toxicity, due to the higher probability of producing $HO^{\bullet}$);
- -intermediate values of both C1 and C3 or C2 and C4 → iron nuclearity = 2 → index value = 0.03 (moderate toxicity);
- -high values of the component C2 (cluster Fe^{II} and Fe^{II}) or C3 (cluster Fe^{III}) → iron nuclearity >2 → index value = 0.02 (low toxicity).

Data on the zeta potential were taken from Pasbakhsh et al. (2013) who investigated a sample from Matauri Bay and found −30 and − 50 mV at pH = 4 and pH = 7, respectively.

3. Results

3.1. Material characterization

The QPAs of the halloysite sample and its graphical output are presented in Table 1 and in Fig. S1 (Appendix A), respectively. It is noteworthy that, based on XRPD, the sample is mostly constituted by halloysite with minor accessory phases (quartz and cristobalite). It should be remarked that the planar disorder of halloysite poses

Table 1
Results of the quantitative phase analysis from XRPD data using the Rietveld method.

Rietveld agreement indices*	
R_p (%)	6.60
R_{wp} (%)	8.36
χ^2	2.18
Phases (wt%)	
halloysite	91.6 ± 0.6
quartz	2.6 ± 0.1
cristobalite	5.8 ± 0.1

* PROFEX v. 5.3.0 software (Döbelin and Kleeberg, 2015).

significant challenges for accurate modelling. Given both this structural complexity and the high halloysite content in the sample, the quantification error may be underestimated. No amorphous phase was detected, being absent or below the detection limit (a few percent).

The calculated weight fraction of halloysite (91.6 wt%) matched the semi-quantitative estimate (87 wt%) reported by Keeling et al. (2015) and Pasbakhsh et al. (2013) on the same Matauri Bay sample. Furthermore, the QPA results are in optimal agreement with the TGA. In fact, as detailed in SM-1 and shown in Fig. S2, the TGA, by distinguish between moisture and interlayer water, indicated that the 10 Å phase occurs in significantly lower amounts than the 7 Å phase (23.4 and 68.1 wt%, respectively). The QPA analyses are also confirmed by major and trace elements content determined by XRF analysis and shown in Table 2. Regarding trace elements, further details will be provided in the discussion (Section 4).

SEM observation highlighted that the sample is composed of micrometer-sized polycrystalline agglomerates/aggregates typically ranging from 5 to 50 μm (Fig. S3a). The individual halloysite particles display both elongated and sub-spherical shapes with sub-micrometric dimension (Fig. S3b). Quartz and cristobalite (sharp particles, better evident in Fig. S3b) are also very small, with mean diameters around 1 μm. SEM/EDS analyses, in agreement with XRF, also indicated the presence of trace phosphates (not shown here) below the detection limit of XRPD.

A gallery of high-resolution TEM pictures of the halloysite sample, showing the sub-micrometric size of the elongated halloysite particles, is shown in Fig. 1. A statistical analysis of the morphometric parameters of the halloysite nanotubus (SM-2) yielded a mean length L of 1.5(0.9) μm, a mean width W of 0.13(0.07) μm, and a mean aspect ratio (L/W) of 13 (9). Further TEM investigation revealed a low (generally below 1 wt%) but widespread distribution of iron in the sample (Fig. 2). Halloysite (recognised from morphology and EDX chemical composition) showed an iron content around 0.2 wt% (Figs. 2a,b and SM-3). Few and small particles of iron oxides of some tenths of nanometres were detected both isolated or on the external surface of halloysite crystals, as shown in Figs. 2c,d and SM-3.

The room temperature Mössbauer spectrum showed a poorly resolved doublet centred at approximately 0.31 mm/s. The best fit (Fit 1) was obtained using two doublets, attributable to Fe^{III} in octahedral coordination. The corresponding hyperfine parameters and the spectrum are reported in Table 3 and Fig. 3a, respectively. Both sites are indicative of Fe^{III} atoms in distorted octahedral coordination. The presence of the second site agrees with literature data (Komusiński et al., 1981) despite the relatively high uncertainty associated to the hyperfine parameters. A single-component model of Fe^{III} was also tested, but did not yield satisfactory results as, without imposing constraints on the parameters, the doublet collapsed into a broadened singlet. The possible presence of Fe^{II} moieties was investigated by using a three components model. The resulting hyperfine parameters (Fit 2) are also presented in Table 3 and the spectrum is shown in Fig. 3b. The existence of the ferrous doublet remains questionable: first, there is no clear evidence of high-velocity absorption; second, the doublet is only observed when the isomer shift and linewidth are fixed.

The UV–Vis pattern of the sample (Fig. 4), with a major band at 257 nm, indicated that Fe^{III} in distorted octahedral coordination is mostly isolated (*e.g.*, nuclearity = 1, iron atoms not connected to other iron atoms through oxygen atoms bridging). In fact, the UV–Vis pattern is comparable to those reported in the literature for phases containing isolated Fe^{III} species in octahedral coordination (Borghi et al., 2010;

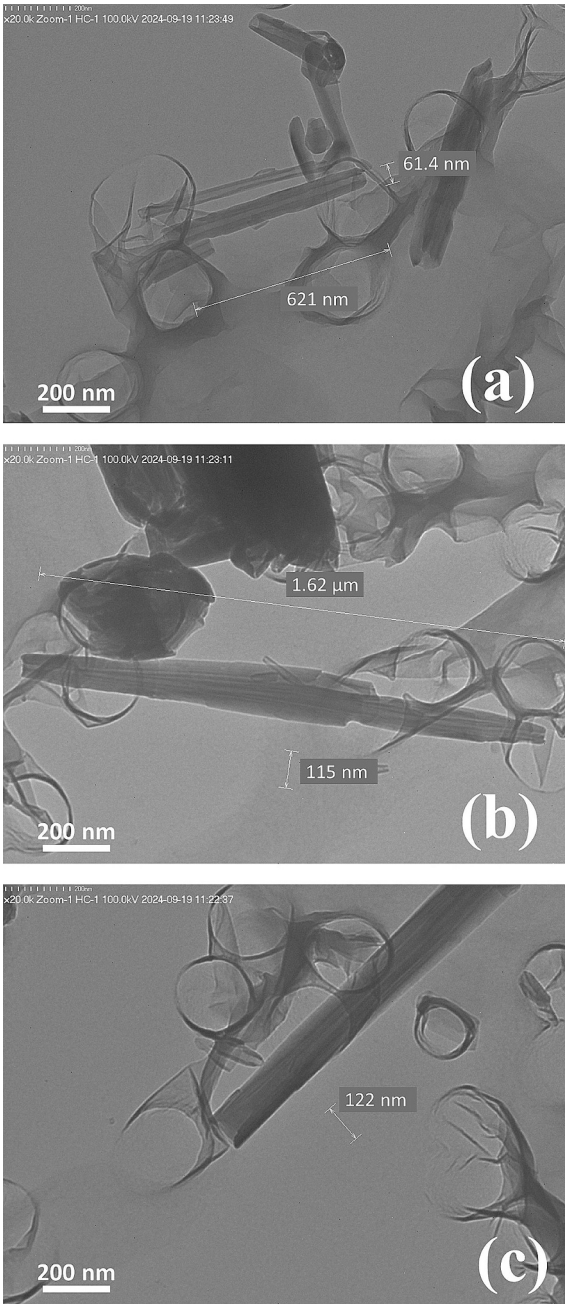

Fig. 1. Selection of TEM images of the halloysite particles. (a) few elongated sub-micrometric particles; (b) an individual halloysite elongated particle; (c) detail of a very thin tube.

Table 2
Major (reported as oxide) and trace elements of the investigated New Zealand halloysite determined from XRF.

Major elements	wt%	Trace elements	ppm	Trace elements	ppm
SiO_2	51.5	F	–	Sr	–
TiO_2	–	S	268	Mo	–
Al_2O_3	33.94	Cl	206	Cd	–
Fe_2O_3	0.30	Sc	11	Sn	27
MnO	–	V	6	Sb	–
MgO	–	Cr	–	Cs	–
CaO	–	Co	2	Ba	15
Na_2O	0.05	Ni	–	Pb	36
K_2O	–	Cu	–	La	12
P_2O_5	0.14	Zn	3	Ce	–
Loss on ignition (L.o.I.)*	14.07	Ga	48	Nd	20
Tot	**100**	As	2	Th	35
		Rb	–	U	7

- = under detection limit; *from TGA data, dehydration water removed (see the text and SM-1for details).

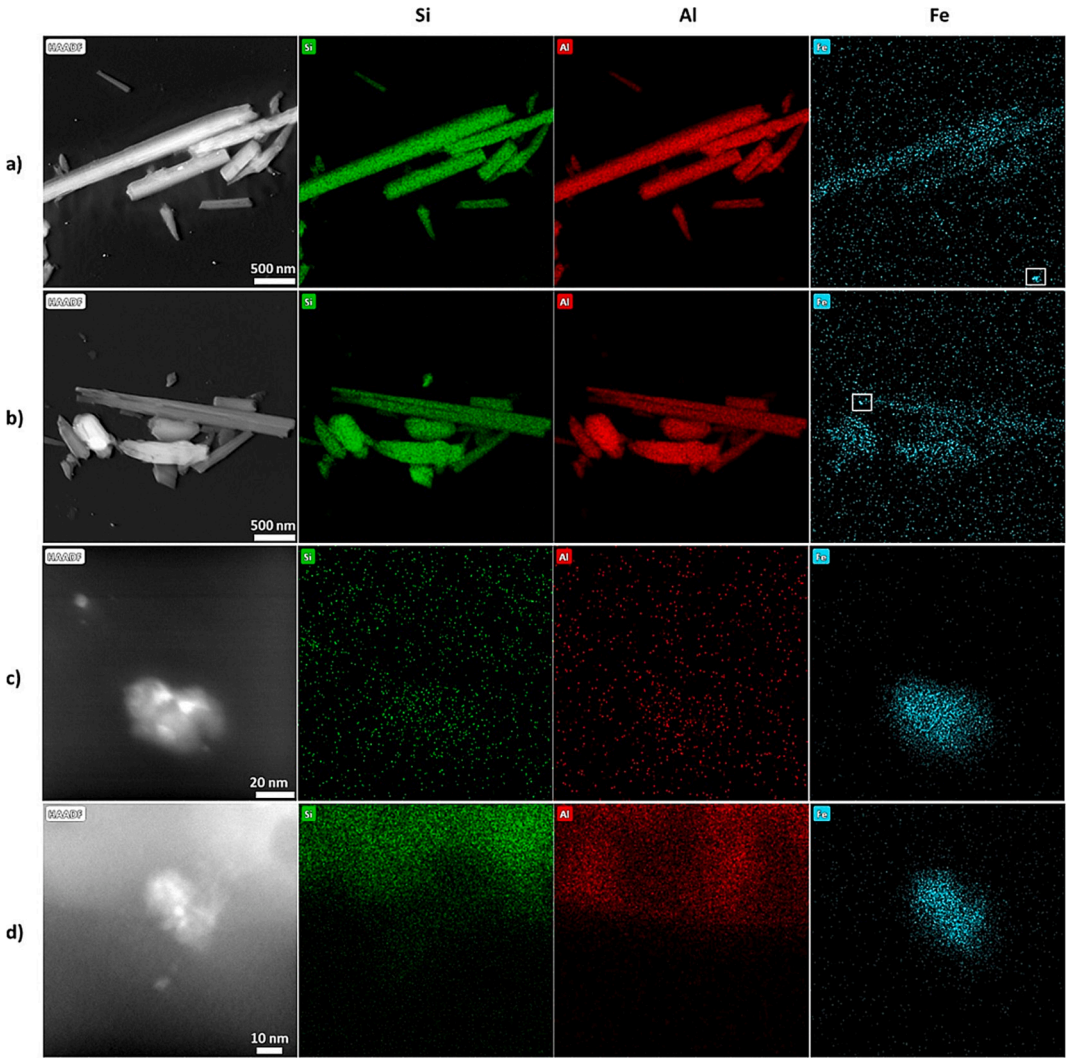

Fig. 2. TEM images in HAADF and Si, Al, Fe distribution in halloysite particles (a, b) and in impurities (c, d) framed in the Fe map of Figs. a and b, respectively.

Table 3
Hyperfine parameters obtained from the room temperature spectrum. δ is quoted to α-Fe.

	δ (mm/s)	Δ (mm/s)	Γ_+ (mm/s)	A (%)	Attribution
			Fit 1		
Site 1	0.30 ± 0.03	0.25 ± 0.05	0.13 ± 0.06	50 ± 5	Fe^{III} M
Site 2	0.38 ± 0.1	1.05 ± 0.3	0.32 ± 0.19	50 ± 5	Fe^{III} M
			Fit 2		
Site 1	0.29 ± 0.03	0.24 ± 0.05	0.13 ± 0.06	54 ± 5	Fe^{III} M
Site 2	0.35 ± 0.08	1.05 ± 0.2	0.23 ± 0.19	38 ± 5	Fe^{III} M
Site 3	0.99*	0.94 ± 0.7	0.2*	8 ± 5	Fe^{II} M

* Constrained parameters.

Pirngruber et al., 2006; Zecchina et al., 2007). The tail from 270 nm to *ca.* 500 nm is indicative of Fe^{III} in a cluster environment of higher nuclearity like that observed for iron oxides and hydroxides (Borghi et al., 2010).

Laser diffraction measurements were performed primarily to obtain a statistically more robust assessment of crystallite size distribution compared to image-based analyses. As shown in Fig. 5, the halloysite particles form rather large agglomerates (5–100 μm), but individual particles are of nanometer size. Hence, a first step involve assessing whether these agglomerates may be properly dispersed to enable accurate measurement *via* light scattering intensity and the Mie Theory. Powders may be dispersed in two different ways, either by dry dispersion using compressed air or wet dispersion using a carrier fluid. The choice of which to use depends not only on practical issues (like sample quantity and incompatibly with carrier liquids), but also on the desired results. For example, size distribution of industrially agglomerated powders, such as spray dried or granulated ones, are measured by dry dispersion units. In contrast, measurement of primary particles in cohesive powders generally includes carrying the particles through the laser beam as a liquid dispersion. A preliminary sieving experiment of a 1 wt% aqueous dispersion showed that no material was retained on a 38 μm sieve, the finest available in the laboratory. The rounded polycrystalline particles seen in the SEM images are thus identified as agglomerates rather than aggregates. Hence, wet dispersion may potentially result in complete dispersion of the polycrystalline agglomerates and thus enable size measurements of the primary particles. The main challenge was to develop suitable sample preparation and measurement protocols that effectively break down agglomerates without breaking the primary particles and prevent flocculation during measurement. The extent to which de-agglomeration is achieved depends on both pre-treatment and measurement conditions. The energy input in terms of mixing and ultrasonication, considering both power and duration, must be optimized with respect to particle size distribution and stability in consecutive measurements. In addition, flocculation can be prevented by using suitable dispersants. For powders composed of

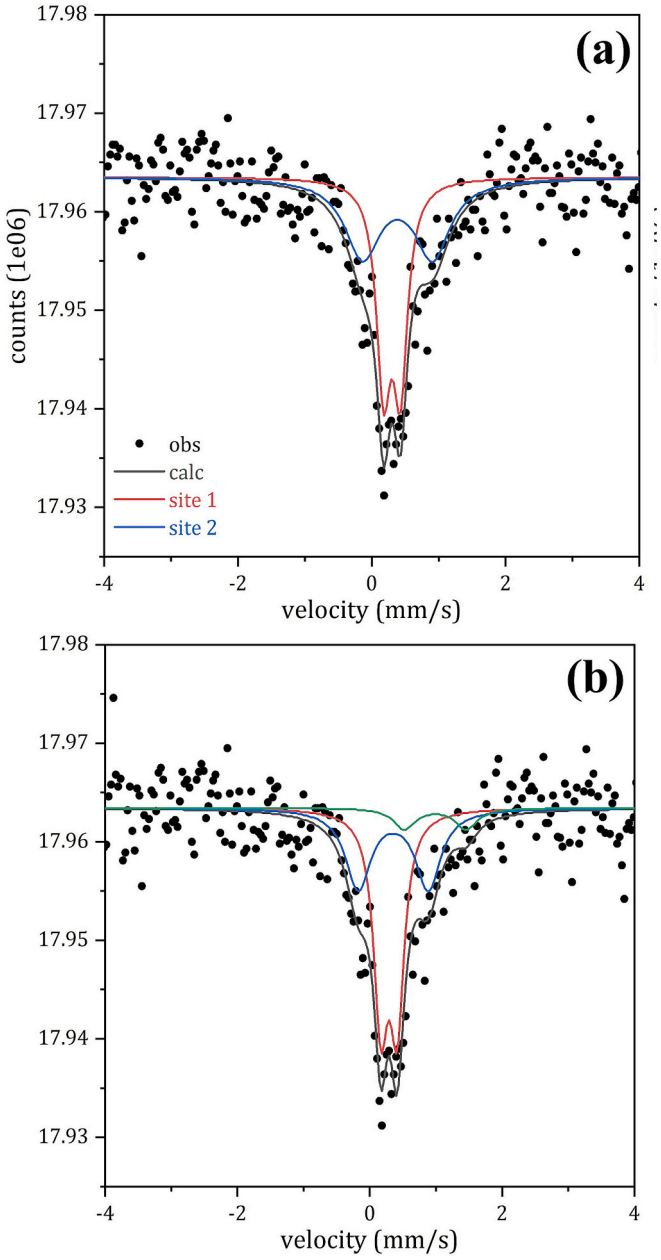

Fig. 3. RT Mössbauer spectrum of halloysite fitted by a two (a) and a three (b) components model.

particles ranging from a few micrometres to nano-scale, prolonged *ex-situ* agitation/ultrasonication in the presence of a deflocculant is generally preferred to break down agglomerate and prevent flocculation of dispersed colloids. In addition, the ultrasonication system integrated in the dispersion unit can also be employed to further achieve fragmentation of agglomerates and flocs, with the advantage of real-time monitoring of the particle size distribution. Deflocculation through the use of additives aims at stabilizing colloids through electrostatic and/or steric stabilization. Common deflocculants for natural colloids such as clays are phosphoric acid derivatives, such as sodium tripolyphosphate (Na-TPF). The phosphate anions adsorb on the particles, thus increasing the negative charge and the Coloumb repulsive forces. In addition, the formation of stable complexes with bi- and trivalent flocculating cations, such as Ca^{2+} and Mg^{2+} and Fe^{3+}, contribute to effective dispersion. With these considerations in mind, a sample preparation protocol was developed by starting with overnight dispersion of the powder in water solution of TPF (Section 2.1). Sequential laser diffraction measurements

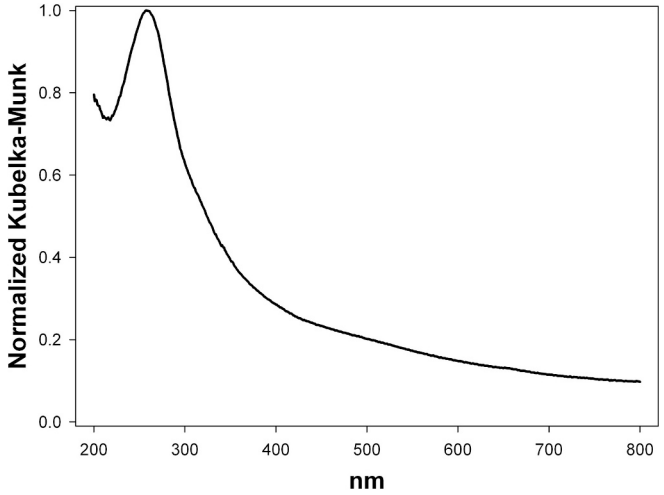

Fig. 4. The UV–Vis spectrum of halloysite in the 200–800 nm range.

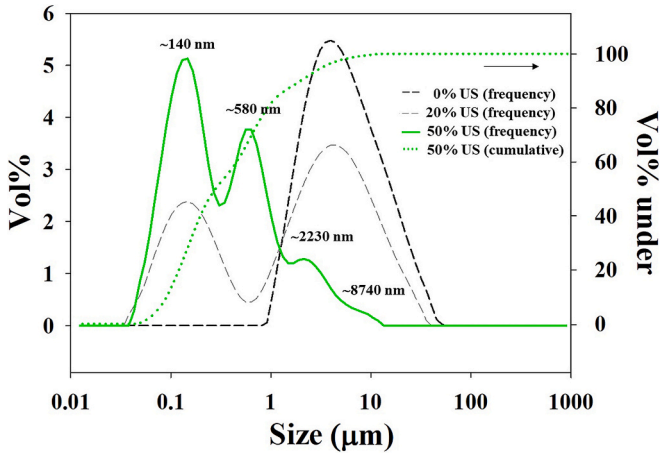

Fig. 5. Particle size distribution measured by laser diffraction. The different curves represent stable consecutive measurements under conditions of different power of ultrasound action (no ultrasound, ultrasound with 20 and 50 % power). The finest distribution was obtained with 50 % ultrasound power (modes, both frequency and cumulative curve, are shown).

were performed in which the power of the ultrasonic equipment implemented in the dispersion unit was successively increased from 0 to 50 %.

The stable size distribution curves obtained using no ultrasonication and ultrasonication with 20 and 50 % power are shown in Fig. 5. As can be observed, the size distribution becomes finer with increased ultrasonication power indicating particle de-agglomeration. Within the time frame of the experiment, 50 % ultrasonic power resulted in highly stable and reproducible results. The final distribution is multimodal with the modes 0.14, 0.58, 2.23 and 8.74 μm. The values of D10, D50 and D90 are 0.091, 0.279 and 1.986 μm, respectively. The first mode at 140 nm probably mirrors the width of the tubular halloysite particles, as this is the smallest dimension among the tubular and sub-spherical particles, align well with TEM results (0.13 ± 0.07 μm, see Fig. 1 and SM-2). The second mode at 0.580 μm was assigned mainly to the subspherical halloysite particles, while the third mode at 1.986 μm corresponds to the length of the tubular halloysite particles. This is also consistent with TEM results (Fig. 1, SM-2), showing a mean length of 1.5 ± 0.9 μm. The minor fourth mode at 8.74 μm is likely indicative of aggregates or agglomerates that were not fully dispersed during sample preparation and measurement.

The value of the measured BET SSA is 26.5(4) m^2/g. To a first

Table 4
The parameters used and the calculated FPTI score for Hal.

Parameter	Classes	Normalized score $FPTI_i$	Halloysite (Matauri Bay, New Zealand)
(1,1) mean fibre length L (μm)	$L \leq 5.0$	0.0	0.0
	$5.0 < L \leq 10.0$	0.1	
	$10.0 < L \leq 20.0$	0.2	
	$L > 20.0$	0.4	
(1,2) mean fibre width D (μm)	$D > 3.0$	0.0	
	$1.0 < D \leq 3.0$	0.1	
	$0.25 < D \leq 1.0$	0.2	
	$D \leq 0.25$	0.4	0.4
(1,3) crystal curvature	flat surface	0.05	
	altered surface	0.1	
	cylindrical surface	0.2	0.2
(1,4) crystal habit	Curled	0.1	
	mixed Curled/acicular	0.2	0.2
	acicular	0.4	
(1,5) fibre density ρ (g/cm^3)	$\rho \leq 2.75$	0.05	0.05
	$2.75 < \rho \leq 3.5$	0.1	
	$\rho > 3.5$	0.2	
(1,6) hydrophobic character of the surface	hydrophobic	0.05	
	amphiphilic	0.1	
	hydrophilic	0.2	0.2
(1,7) specific surface area SSA (m^2/g)	$SSA > 25.0$	0.05	0.05
	$5.0 < SSA \leq 25.0$	0.1	
	$SSA \leq 5.0$	0.2	
(1,8) total iron content $Fe_2O_3 + FeO$ (wt%)	$Fe_2O_3 + FeO = 0.0$ (no iron)	0.0	
	$0 < Fe_2O_3 + FeO \leq 1$	0.05	0.05
	$1 < Fe_2O_3 + FeO \leq 10$	0.1	
	$Fe_2O_3 + FeO > 10$	0.2	
(1,9) ferrous iron FeO (wt%)	$FeO = 0.0$ (no ferrous iron)	0.0	0.0
	$0.0 < FeO \leq 0.25$	0.05	
	$0.25 < FeO \leq 1.0$	0.1	
	$FeO > 1.0$	0.2	
(1,10) nuclearity or iron atoms n	$n = 0$ (no iron atoms)	0.0	
	$n > 2$	0.02	
	$n = 2$	0.03	
	$n = 1$	0.07	0.07
(1,11) content of metals other than iron [(1)] (ppm/ppm)	$\sum_i \frac{C_i}{L_i} = 0.0$ (no metals)	0.0	
	$0.0 < \sum_i \frac{C_i}{L_i} \leq 1.0$	0.1	
	$1.0 < \sum_i \frac{C_i}{L_i} \leq 5.0$	0.2	0.2
	$\sum_i \frac{C_i}{L_i} > 5.0$	0.4	
(1,12) fibre dissolution time t [(2)] (y)	$t \leq 1.0$	0.05	
	$1 < t \leq 40.0$	0.1	0.1
	$t > 40.0$	0.2	
(1,13) velocity of iron release v_R [(3)] (wt%/y)	$v_R = 0.0$ (no iron)	0.0	
	$0.0 < v_R \leq 0.1$	0.03	0.03
	$0.1 < v_R \leq 1$	0.07	
	$v_R > 1$	0.13	
(1,14) velocity of silica dissolution v_S [(4)] (wt%/y)	$v_S = 0.0$ (no silica)	0.0	
	$0.0 < v_S \leq 0.5$	0.02	
	$0.5 < v_S \leq 1.0$	0.03	
	$v_S > 1.0$	0.07	0.07
(1,15) velocity of release of metals v_M [(5)] (ppm/y)	$v_M = 0.0$	0.0	
	$0.0 < v_M \leq 1.0$	0.03	
	$1.0 < v_M \leq 10.0$	0.07	0.07
	$v_M > 10.0$	0.13	
(1,16) zeta potential ζ (mV)	(−) at pH = 4.0–4.5	0.1	
	(−) at both pH = 4.0–4.5 and 7.0–7.4	0.2	0.2

(*continued on next page*)

Table 4 (*continued*)

Parameter	Classes	Normalized score $FPTI_i$	Halloysite (Matauri Bay, New Zealand)
(1,17) ζ values [6] inducing fibres aggregation (mV)	$\zeta > 20.0$ or $\varsigma < -20.0$	0.03	0.03
	$10.0 < \zeta \leq 20.0$ or $-20.0 \leq \zeta < -10.0$	0.07	
	$0.0 \leq \zeta \leq 10.0$ or $-10.0 \leq \zeta \leq 0.0$	0.13	
(1,18) cation exchange	cation exchange	0.07	
	no cation exchange	0	0.0
		FPTI (error) [7]	**1.92(0.10)**

[1] $\sum_i \frac{C_i}{L_i}$=sum of the concentrations of heavy metals (Sb, As, Hg, Cd, Co, Cr, Cu, Pb, Ni, Zn, V, Be) C_i in the fibre (ppm) divided by the limit L_i for that metal according to the existing regulatory system (Tóth et al., 2016) except for Be with limit = 0.5 ppm;
[2] the total dissolution time of the fibre calculated in years (y) following the standardized acellular *in vitro* dissolution model at pH = 4.5 described in Gualtieri et al. (2018);
[3] total content of elemental iron in the fibre (wt%) possibly made available as active iron at the surface of the fibre divided by the total dissolution time (y) of the fibre;
[4] total content of Si of the fibre (wt%) divided by the total dissolution time (y) of the fibre;
[5] total content (ppm) of heavy metals (Sb, As, Hg, Cd, Co, Cr, Cu, Pb, Ni, Zn, V, Be, Mn) divided by the total dissolution time (y) of the fibre;
[6] at the pH = 7.4 of the extracellular environment.
[7] calculated ad reported in the WebFPTI manual freely available at https://fibers-fpti.unimore.it/FPTI/.

approximation, the large surface area favours the dissolution of the Hal particles, making them less biodurable and consequently less toxic.

3.2. Calculation of the FPTI model

The parameters used and the FPTI score of Hal are reported in Table 4. The FPTI value 1.92(0.10) calculated using the WebFPTI applicative (Gualtieri et al., 2021; WebFPTI manual available at https://fibers-fpti.unimore.it/FPTI/) will be further discussed through comparison with values available for both positive (carcinogenic) and negative (non-carcinogenic) standard mineral fibres.

4. Discussion

The chemical, mineralogical and morphometric data of investigated Hal sample are consistent with those reported in the existing literature (see for example, Christie et al., 2000; Levis and Deasy, 2002; Pasbakhsh et al., 2013; Keeling et al., 2015; Wilson and Keeling, 2016; Lampropoulou and Papoulis, 2021). One exception is the measured value of SSA (26.5(4) m^2g^{-1}), slightly greater than the value (22.1 m^2g^{-1}) reported by Pasbakhsh et al. (2013). This beneficiated sample contains about 90 wt% halloysite clay with minor silica phases (quartz and cristobalite) and other impurities below the detection limit of XRPD. The nature of the geomaterial and the processing of the ore result in a product with a very high clay content. Brathwaite et al. (2012) and Wilson and Keeling (2016) explained that the Matauri Bay halloysite contains fewer impurities compared to other halloysites, because the Matauri Bay deposit formed by weathering in equilibrium with meteoric waters, rather than by acid-sulphate hydrothermal alteration. This minerogenesis is witnessed by the simple mineral assemblage, absence of sulphate and phosphate minerals, and hydrogen/oxygen isotope composition. The small amount of titanium in the sample, a common feature of these halloysite- and kaolinite-rich clays, have been assigned to oxides, such as TiO_2 in the form of anatase (Joussein et al., 2005 and references therein).

The nature of the minor iron content of the Matauri Bay halloysite samples has been subject of debate in the literature. Spectroscopic data published by Coyne et al. (1989) basically showed that Matauri Bay halloysite displays O-centres connected to structural iron. Chaikum and Carr (1987) reported that the resonance at g = 5 is due to Fe^{III} atoms in an octahedral site which is influenced by interactions between hydroxyl groups of the octahedral sheet. Watanabe et al. (1969) assumed some irregular replacement of Al^{III} by Fe^{III} in octahedral positions. Similarly, Joussein et al. (2005) and references therein reported that evidences in the literature point to associated iron oxides such as hematite or maghemite, and partly to isomorphous substitution of Fe^{III} for Al^{III} in the octahedral sheet. These authors also reported that isomorphous heterovalent substitution of Fe^{III} for Si^{IV} in the tetrahedral sheet has never been pointed out for halloysite. TEM (Fig. 2 and SM-3) and Mössbauer data (Fig. 3 and Table 3) discussed here finally explained the nature of iron in Matauri Bay halloysite, showing that Fe^{III} atoms are found in distorted octahedral sites in place of Al^{III} atoms inside the lattice of halloysite and in distorted octahedral coordination in impurities of oxides or hydroxides (hematite or goethite). A very minor, if any, content of Fe^{II} can also be hosted in the same distorted octahedral sites (see fit 2 in Table 3).

The low content of iron of the Matauri Bay halloysite apparently influences its crystal shape and curvature. Bailey (1990) found that the iron content is negatively correlated with the layer curvature of halloysite. As the degree of $Fe^{III} \rightarrow Al^{III}$ replacement increases, the layer curvature decreases, which in turn affects the crystal and particle morphology of halloysite. Platy particles always contain a relatively high amount of iron, while tubular particles lack iron (Joussein et al., 2005; Huang et al., 2024). Morphometric data (Fig. 1, SM-2) seems to confirm this model as the sample is mostly composed of halloysite nanotubes with mean L = 1.5(0.9) μm, W = 0.13(0.07) μm, and L/W = 13(9). The size of the halloysite nanotubes is within the ranges reported in the literature. In fact, the lengths of halloysite nanotubes cover a wide range from 0.02 to >30 μm, while their widths range from <0.05 to 0.2 μm (Joussein et al., 2005 and references therein). It is important to emphasize that halloysite exhibits a complex morphology of the nanotubes. Gray-Wannell et al. (2023) clarified that the widely accepted model of Hal as a 'carpet roll' nanotube is overly simplistic, and that many technological applications aiming to functionalize Hal might benefit from considering more realistic models. Their TEM data showed that for both cylindrical and prismatic halloysite forms, the mean diameter of the central lumen is about 12 nm. Gray-Wannell et al. (2023) also reported that the central lumen is the primary nano-confined pore space in cylindrical Hal, but in prismatic forms additional slit-shaped pores of a wide variety of sizes are present between layer packets, particularly at the interfacial junction between the cylindrical core and the outer planar sectors.

For the aims of this work, it is important to classify the particles composing Hal on the basis of their morphology:

- They are "elongate mineral particles" (EMPs) because, according to the definition ("Any mineral particle with a L/W (aspect ratio) of 3:1 or greater assuming the width of a particle to be an apparent parameter defined as the longest dimension of the particle in the

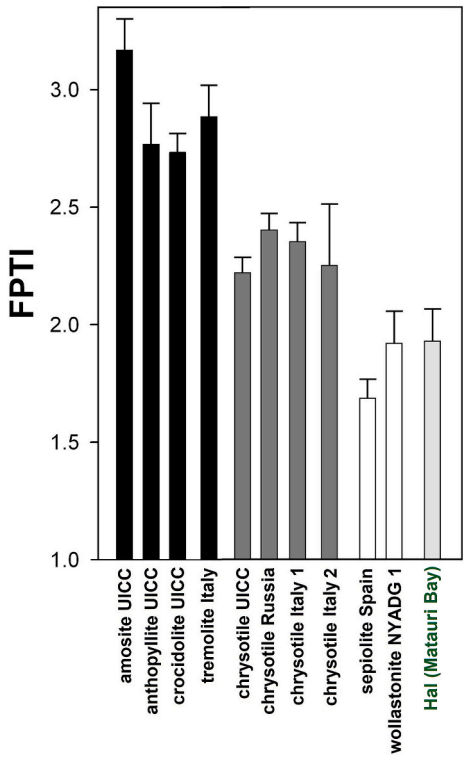

Fig. 6. The calculated FPTI value of halloysite from Matauri Bay compared to those of amphibole asbestos, chrysotile, sepiolite, and wollastonite mineral fibres. From left to right are reported: carcinogenic amphibole asbestos fibres standard amosite UICC, with FPTI value of 3.17(0.14), Gualtieri, 2018; standard asbestos anthophyllite UICC, 2.77(0.18), Gualtieri, 2018; standard crocidolite UICC, 2.73(0.09), Di Giuseppe et al., 2021a; asbestos tremolite from Val D'Ala (Italy), 2.88(0.14), Gualtieri, 2018); carcinogenic chrysotile fibres UICC standard, 2.22(0.08), Di Giuseppe et al., 2021b; Russian chrysotile commercial sample with L > 5 μm, 2.35(0.06), Di Giuseppe et al., 2021a; Balangero (Italy 1), 2.35(0.09) and Valmalenco (Italy 2), 2.25(0.26), Di Giuseppe et al., 2021a; non-carcinogenic sepiolite fibres from Spain, 1.68(0.09), Gualtieri, 2018; NYAD G 1 wollastonite, 1.92(0.15), Di Giuseppe et al., 2021b); Hal Matauri Bay (this study), 1.92(0.10). References are only for sample description as in most cases the FPTI values and/or errors were updated (see https://fibers-fpti.unimore.it/FPTI/materials/) with minor changes.

plane perpendicular to length and the shortest dimension of the two-dimensional outline of a particle": NIOSH, 2011), their L/W ≥ 3.

- They are respirable ("the mass fraction of inhaled particles penetrating to the unciliated airways (Brown et al., 2013), usually with W ≤ 3 μm or with aerodynamic diameter ≤ 2.5 μm (PM2.5)/≤4.0 μm (PM4").
- Although respirable, they are not "regulated fibres" because, according to the World Health Organization (WHO) indicating the following counting criteria to classify regulated (respirable) fibres: L ≥ 5 μm, W ≤ 3 μm, L/W ≥ 3:1 (Belluso et al., 2017), their L < 5 μm.
- From a regulatory standpoint, *e.g.* the current standard NIOSH Method 7400 that only counts EMPs >5 μm in length and ≥ 3 in aspect ratio, these particles should not be considered.
- This material is not "asbestos" and halloysite has never been evaluated by the IARC as potential carcinogenic agent.

In accordance with regulatory classification, the potential toxicity of Hal was assessed using the FPTI model. No biological assessment of toxicity of Hal was conducted in this study, as the focus regards the assessment of the potential toxicity based solely on the chemical-physical parameters of the particles. Overall, the prediction of a low toxicity of Hal from the FPTI model is in concert with findings of existing literature. As noted in the Introduction, previous studies consistently indicated that halloysite, including Hal samples, is non-toxic (Vergaro et al., 2010; Chiriacò et al., 2014; Sánchez-Fernández et al., 2014; Fakhrullina et al. (2015); Liu et al., 2015; Maisanaba et al., 2015; Jaurand, 2016; Brandelli, 2018; Long et al. (2018); Massaro et al., 2018b; Santos et al. (2019); Barfod et al. (2020); Wu et al. (2020); Rozhina et al., 2021; Biddeci et al., 2023). Limited toxicity has been reported only at high/very high doses (Ahmed et al., 2015; Fakhrullina et al., 2015; Zhao et al. (2019); Lazzara et al., 2023). Adverse effects *in vivo* have been observed for applications other than inhalation, namely in drug delivery and bio-imaging applications (Leporatti et al., 2020) and oral administration in mice (Wang et al., 2018). To the authors' knowledge, only the *in vivo* study of Rong et al. (2019) evaluated the toxicity of inhaled Hal and found that they can cause sub-chronic toxicity in mice. Few *in vitro* studies reported cytotoxic effects in cell cultures of the respiratory system (Luo et al., 2020; Sawicka et al., 2021) and need more robust experimental evidence.

The FPTI values of fibres evaluated by IARC as "carcinogenic" (amphibole asbestos and chrysotile) or "with inadequate evidence of carcinogenicity to humans" (sepiolite and wollastonite) are shown in Fig. 6. The calculated FPTI value of 1.92(0.10) of Hal (Table 4) is comparable to those reported for sepiolite and wollastonite mineral fibres. The parameter in the potential toxicity model that most decreases the overall score for halloysite is the short size (parameter (1,1) L = 1.5 (0.9) μm) of the fibres, which can successfully undergo clearance by the alveolar macrophages (Stanton et al., 1981; Donaldson et al., 2010; Gualtieri, 2023). Numerous studies have confirmed that size is a key factor in determining the carcinogenicity potential of mineral fibres like "asbestos" fibres (Wylie et al., 2022). In particular, shorter fibres (*e.g.*, with length < 5 μm) are considered to pose little or no carcinogenic effect (Bernstein, 2022). Although systematic and consistent data are currently lacking to fully support this argument, it should be remarked that some authors have questioned the "short asbestos fibre toxicity paradigm". Boulanger et al. (2014) for example, claimed that pathogenicity of short asbestos fibres cannot be completely ruled out, especially under conditions of high exposure. On the other hand, the very small width (W = 0.13(0.07) μm) is a parameter that plays a key role in toxicity, inflammatory potential, carcinogenicity, and fibrogenic potential of mineral fibres; in fact, it is relevant in defining the equivalent aerodynamic diameter and influences pulmonary and pleural deposition (Donaldson et al., 2010; Gualtieri et al., 2017).

Concerning the parameter (1,3), the cylindrical surface of the nanoparticles can be a detrimental factor as protein adsorption on curved surfaces or nanoparticles is unfavoured (Lynch and Dawson, 2008; Gualtieri, 2018). This reduced adsorption limits the activation of protein-mediated biochemical mechanisms that would otherwise counteract the surface activity of the fibres. Compared to needle-like fibres like amphibole asbestos, a mixed needle-like/curled crystal shape (parameter (1,4)) of the halloysite fibres is likely to promote, at least in part, the deposit in the upper airways system where they are taken up by the epithelial cells and translocated to the interstitium or cleared through the mucociliary elevator (Evans et al., 1973; Gualtieri, 2018).

The low density (parameter (1,5)) of halloysite is a positive factor. Although the effect is limited for particles of such small size, lower density increases the aerodynamic diameter, thereby reducing the depth of fibres deposition in the respiratory tract, since denser fibres tend to penetrate more deeply (Gualtieri et al., 2017). Concerning the hydrophilic character of the surface (parameter (1,6)), it is well established that hydrophobic surfaces adsorb biopolymers more strongly than hydrophilic surfaces (van Oss et al., 1999). Moreover, particles with stronger hydrophobic character, not the case for halloysite, are generally more prone to cell uptake (Gualtieri, 2018).

The content of iron and metals (parameters (1,8) and (1,11), respectively) of the halloysite fibres is very small, as well as ferrous iron is negligible (parameter (1,9)). Hence, metals driven Fenton primary production of cyto−/geno-toxic hydroxyl radical HO•, which is responsible for the toxicity and carcinogenicity of respirable mineral

fibres (Gualtieri et al., 2024), should be minor. Nevertheless, iron species in the halloysite lattice are present as isolated (monomeric) sites, which are expected to serve as preferred catalytic centres for the production of hydroxyl radical HO• (Koppenol and Hider, 2019). This contrast with paired Fe-O-Fe active species, Fe_xO_y clusters or clustered iron with high nuclearity which typically exhibit reduced or null activity (iron nuclearity is the parameter (1,10) in the model).

Based on the dissolution data available for kaolinite (Yang and Steefel, 2008), the dissolution time (parameter (1,12)) of halloysite at pH = 4 was calculated for an ideal 0.25 μm thick fibre, following the method reported in Gualtieri et al. (2018). It is assumed that fibres which dissolve rapidly in lung fluids, exhibit low biopersistence and are therefore, in principle, less harmful than biopersistent fibres. The estimated value of 1.18 y is longer than that of non-biodurable chrysotile, but much shorter than that of highly biodurable fibres like amphibole asbestos and erionite (Gualtieri et al., 2018). The dissolution of the halloysite particles is also favoured by the high SSA of 26.5(4) m^2g^{-1} (parameter (1,7)). Fibre dissolution time influences the release of iron, metal ions, and silica species *in vitro/in vivo* (respectively parameters (1,13), (1,15), and (1,16) in the model), eventually making these species available at the fibre surface to catalyze Fenton like reactions and promote the intracellular or extracellular generation of detrimental reactive species.

Data on the zeta potential (parameter (1,16) of this sample were taken from the literature (Pasbakhsh et al., 2013). The negative values of −30 and − 50 mV at pH = 4 and pH = 7, respectively, may correlate with a number of phenomena responsible for adverse effects *in vivo*, and are comparable to those displayed by mineral fibres at pH 4–4.5 and 7 (Pollastri et al., 2014). Halloysite displays high (<−20) absolute values of the zeta potential with particles that are expected to be well dispersed in fluids. In fact, it is known that when particles have low absolute values of the zeta potential (> − 20 or < 20), particle agglomeration (parameter (1,17) is favoured (see for example, Pochapski et al., 2021). In the case of mineral fibres, those with low absolute values of zeta potential (*i.e.*, agglomerated fibres) are virtually more prone than fibres with high absolute values (*i.e.*, stable) to cause adverse effects such as frustrated phagocytosis (Gualtieri, 2018 and references therein).

A notable concern regarding halloysite from Matauri Bay is the presence or respirable crystalline silica (RCS) in the form of quartz and cristobalite (Table 1). SEM/TEM data showed that both quartz and cristobalite particles are very small in size, with mean diameters of approximately 1 μm, making them respirable. RCS is known to cause silicosis and lung cancer and has been classified as a known human carcinogen (*Group 1*) by the IARC Monographs Program in 1997 and 2012 (Steenland and Ward, 2014). Recently, there has been growing concern about workers' exposure to manufacture processes of natural raw materials that produce dusts because they contain RCS. Special attention is paid to activities such as movement of earth (*e.g.*, mining, oil/gas extraction, hydraulic fracturing, farming, construction, quarrying), as well as the disturbance, handling or use of crystalline silica containing materials; these include, for example, quartz sand or other crystalline silica-containing products and materials used in the manufacturing, finishing and installing of natural and engineered or artificial stone products (IARC, 2012; Boers, 2024).

The latter activities drew great concern because of recent cases of silicosis and other respiratory diseases recorded in various countries among workers involved in machining silica-containing countertops (Boers, 2024; Molinari et al., 2024 and references therein). Concern about RCS have prompted a strong global response, with many countries having regulated occupational exposure to this agent for over a decade. Moreover, several others are currently in the process of revising existing regulations and guidelines. For example, the US Occupational Safety and Health Administration (OSHA) has proposed updated regulations for lowering the permissible occupational limit for crystalline silica (Steenland and Ward, 2014). More recently, the US Mine Safety and Health Administration (MSHA) amended its standards to better protect miners exposed to RCS (MSHA, 2024). In addition, US California/OSHA implemented a Special Emphasis Program and Emergency Temporary Standard to strengthen consultation and enforcement efforts. These measures specifically target workplaces performing high-exposure tasks involving engineered or natural stones containing more than 10 wt% crystalline silica (Jones and Batteate, 2024). The Australian Government has issued guidelines to protect workers and others in the workplace from exposure to RCS (SWA, 2024). Furthermore, in 2024 Australia implemented a ban on engineered stone products containing more than 1 wt% crystalline silica (Jones and Batteate, 2024). In light of this regulatory context, crystalline silica-rich halloysite, such the sample investigated in this study, should be manged with the same level of care and precaution as other crystalline silica-rich natural raw materials. For instance, safe work with halloysite should consider the ACGIH TWA concentration limit of 0.1 mg/m^3 for respirable dust, as well as the OSHA PEL (TWA) concentration limit of 15 mg/m^3 in the workplace environment. In this regard, the case of the lithium mine workers in Western Australia, where operations are mainly located in quartz-rich pegmatite deposits, offer an instructive precedent (Gbondo et al., 2024).

5. Conclusions

The chemical-physical and mineralogical properties of a commercial sample of natural halloysite from New Zealand, used in the manufacture of ceramic products, were investigated to assess its potential toxicity. Halloysite has not been assessed by IARC as a potential carcinogenic agent. This beneficiated sample contains approximately 90 wt% halloysite clay, along with quartz and cristobalite, and is free from asbestos contamination.

TEM and Mössbauer spectroscopy data revealed that Fe^{III} atoms are located in distorted octahedral sites, substituting Al^{III} atoms within the halloysite lattice, as well as in impurities of oxides and hydroxides.

The sample contains respirable "elongate mineral particles" (EMPs). Although these particles are respirable, they are not classified as "regulated fibres" by the World Health Organization (WHO) since their length (L < 5 μm) falls below the regulatory threshold. For example, under current standards such as NIOSH Method 7400, these particles are not considered regulated fibres.

Potential toxicity was assessed using the FPTI model, which yielded a calculated FPTI value of 1.92(0.10), comparable to that of mineral fibres with inadequate evidence of carcinogenity for humans. The primary factor reducing the overall toxicity score for halloysite is the short fibre length (L = 1.5(0.9) μm), which allows efficient clearance by alveolar macrophages. Additionally, the very low iron and metal content further reduces toxicity. Consequently, the production of cyto−/geno-toxic HO• through metal-driven Fenton reactions, a key mechanism underlying the toxicity and carcinogenicity of respirable mineral fibres, is expected to be minimal. It is worth noting, however, that iron species within the halloysite lattice exist as isolated (monomeric) sites, which may serve as preferential catalytic centres for HO• production.

The findings of this study are therefore consistent with existing literature indicating that halloysite, particularly halloysite nanotubes (Hal), is a safe, low-toxicity nanomaterial, with no urgency of reclassification. This is in line with the designation of halloysite as safe by the U. S. FDA. Nonetheless, the precautionary stance advocated by Koivisto et al. (2018) is firmly supported, as they recommend avoiding inhalation exposure to Hal due to the limited toxicological information currently available.

A significant concern with halloysite from Matauri Bay is the presence of respirable crystalline silica, comprising 8.4 wt% quartz and cristobalite. The natural product undergoes extensive processing to reduce fine-grained silica content. However, these processing methods are insufficient to eliminate the fine crystalline silica fraction. Advanced wet sedimentation of the raw material may be a more effective approach. Therefore, the handling of halloysite from Matauri Bay should comply with established occupational safety guidelines.

CRediT authorship contribution statement

Alessandro F. Gualtieri: Writing – original draft, Visualization, Validation, Supervision, Project administration, Investigation, Funding acquisition, Conceptualization. **Laurie Glossop:** Writing – original draft, Visualization, Validation, Resources, Investigation, Conceptualization. **Daniele Malferrari:** Writing – original draft, Visualization, Validation, Project administration, Investigation, Funding acquisition, Conceptualization. **Elena Castellini:** Writing – original draft, Visualization, Validation, Investigation, Conceptualization. **Magdalena Lassinantti Gualtieri:** Writing – original draft, Visualization, Validation, Investigation, Conceptualization. **Miriam Hanuskova:** Writing – original draft, Visualization, Validation, Resources, Investigation, Conceptualization. **Luca Nodari:** Writing – original draft, Visualization, Validation, Investigation, Conceptualization. **Jordan Ogor:** Writing – original draft, Visualization, Validation, Resources, Investigation, Conceptualization. **Riccardo Fantini:** Writing – original draft, Visualization, Validation, Investigation, Conceptualization.

Declaration of competing interest

The authors declare that they have no known competing financial interests or personal relationships that could have appeared to influence the work reported in this paper.

Acknowledgments

This work was funded under: i) ECOSISTER: National Recovery and Resilience Plan (NRRP), Mission 04 Component 2 Investment 1.5 - NextGenerationEU, Call for tender n. 3277 dated 30/12/2021; Award Number: 0001052 dated 23/06/2022; ii) PRIN2022 “SEEDS - Sediments Eco-recycling Exploitation, Development and Sustainability” – Project Code 2022BCL34N, Finanziato dall’Unione europea- Next Generation EU, Missione 4 Componente 1 CUP-E53D23004330006.

Appendix A. Supplementary data

Supplementary data to this article can be found online at https://doi.org/10.1016/j.clay.2025.107917.

Data availability

Data will be made available on request.

References

Ahmed, F.R., Shoaib, M.H., Azhar, M., Um, S.H., Yousuf, R.I., Hashmi, S., Dar, A., 2015. *In-vitro* assessment of cytotoxicity of halloysite nanotubes against HepG2, HCT116 and human peripheral blood lymphocytes. Colloids Surf. B: Biointerfaces 135, 50–55.

Bailey, S.W., 1980. Structures of Layer Silicates. In: Brindley, G.W., Brown, G. (Eds.), Crystal Structures of Clay Minerals and Their X-Ray Identification. Mineralogical Society of Great Britain and Ireland, Colchester and, London, pp. 1–124.

Bailey, S.W., 1990. Halloysite - a critical assessment. In: Structure, Surface Chemistry, Farmer, V.C., Tardy, Y. (Eds.), Mixed Layering of Clays. Proceedings of the 9th International Clay Conference 1989. Sciences Géologiques, Mémoire 86, Strasbourg, France, pp. 89–98.

Barfod, K.K., Bendtsen, K.M., Berthing, T., Koivisto, A.J., Poulsen, S.S., Segal, E., Verleysen, E., Mast, J., Holländer, A., Alstrup Jensen, K., Sørig Hougaard, K., Vogel, U., 2020. Increased surface area of halloysite nanotubes due to surface modification predicts lung inflammation and acute phase response after pulmonary exposure in mice. Environ. Toxicol. Pharmacol. 73, 103266.

Belluso, E., Cavallo, A., Halterman, D., 2017. Crystal habit of mineral fibres, chapter 3. In: Gualtieri, A.F. (Ed.), Mineral Fibres: Crystal Chemistry, Chemical-Physical Properties, Biological Interaction and Toxicity, vol. 18. European Mineralogical Union - EMU Notes in Mineralogy, pp. 65–109.

Bernstein, D.M., 2022. The health effects of short fiber chrysotile and amphibole asbestos. Crit. Rev. Toxicol. 1–24.

Bessa, M.J., Brandão, F., Viana, M., Gomes, J.F., Monfort, E., Cassee, F.R., Fraga, S., Teixeira, J.P., 2020. Nanoparticle exposure and hazard in the ceramic industry: an overview of potential sources, toxicity and health effects. Environ. Res. 184, 109297.

Biddeci, G., Spinelli, G., Colomba, P., Di Blasi, F., 2023. Nanomaterials: a review about halloysite nanotubes, properties, and application in the biological field. Int. J. Mol. Sci. 23 (19), 11518.

Boers, D., 2024. Respirable crystalline silica. Arbete Och Hälsa (work and Health). Sci. Ser. 58 (2), 1–129.

Borghi, E., Occhiuzzi, M., Foresti, E., Lesci, I.G., Roveri, N., 2010. Spectroscopic characterization of Fe-doped synthetic chrysotile by EPR, DRS and magnetic susceptibility measurements. Phys. Chem. Chem. Phys. 12 (1), 227–238.

Boulanger, G., Andujar, P., Pairon, J.C., Billon-Galland, M.A., Dion, C., Dumortier, P., Brochard, P., Sobaszek, A., Bartsch, P., Paris, C., Jaurand, M.C., 2014. Quantification of short and long asbestos fibers to assess asbestos exposure: a review of fiber size toxicity. Environ. Health 13, 1–18.

Brandelli, A., 2018. Toxicity and safety evaluation of nanoclays. Nanomaterials: Ecotoxicity, safety, and public perception. In: Rai, M., Biswas, J. (Eds.), Nanomaterials: Ecotoxicity, Safety, and Public Perception. Springer, Cham, pp. 57–76.

Brathwaite, R.L., Christie, A.B., Faure, K., Townsend, M.G., Terlesk, S., 2012. Origin of the Matauri Bay halloysite deposit, Northland. New Zealand. Mineralium Dep. 47, 897–910.

Brown, J.S., Gordon, T., Price, O., Asgharian, B., 2013. Thoracic and respirable particle definitions for human health risk assessment. Particle Fibre Toxicol. 10 (1), 1–12.

Chaikum, N., Carr, R.M., 1987. Electron spin resonance studies of halloysites. Clay Miner. 22 (3), 287–296.

Chiriacò, F., Conversano, F., Sbenaglia, E.A., Casciaro, S., Leporatti, S., Lay-Ekuakille, A., 2014. Cytotoxicity measurements of Halloysite Nanotubes for nanomedicine applications. In: 2014 IEEE International Symposium on Medical Measurements and applications (MeMeA), pp. 1–4.

Christie, T., Douch, C., Winfield, B., Thompson, B., 2000. Industrial Minerals in New Zealand. New Zealand Mining. 27, 14–25.

Coyne, L.M., Costanzo, P.M., Theng, B.K.G., 1989. Luminescence and ESR studies of relationships between O−-centres and structural iron in natural and synthetically hydrated kaolinites. Clay Miner. 24 (4), 671–693.

Di Giuseppe, D., Harper, M., Bailey, M., Erskine, B., Della Ventura, G., Ardit, M., Pasquali, L., Tomaino, G., Ray, R., Mason, H., Dyar, M.D., Hanuskova, M., Giacobbe, C., Zoboli, A., Gualtieri, A.F., 2019. Characterization and assessment of the potential toxicity/pathogenicity of fibrous glaucophane. Environ. Res. 178, 108723.

Di Giuseppe, D., Zoboli, A., Nodari, L., Pasquali, L., Sala, O., Ballirano, P., Malferrari, D., Raneri, S., Hanuskova, M., Gualtieri, A.F., 2021a. Characterization and assessment of the potential toxicity/pathogenicity of Russian commercial chrysotile. Am. Mineral. 106 (10), 1606–1621.

Di Giuseppe, D., Scognamiglio, V., Malferrari, D., Nodari, L., Pasquali, L., Lassinantti Gualtieri, M., Scarfì, S., Mirata, S., Tessari, U., Hanuskova, M., Gualtieri, A.F., 2021b. Characterization of fibrous wollastonite NYAD G in view of its use as negative standard for *in vitro* toxicity tests. Minerals 11 (12), 1378.

Döbelin, N., Kleeberg, R., 2015. Profex: a graphical user interface for the Rietveld refinement program BGMN. J. Appl. Crystallogr. 48, 1573–1580.

Donaldson, K., Murphy, F.A., Duffin, R., Poland, C.A., 2010. Asbestos, carbon nanotubes and the pleural mesothelium: a review of the hypothesis regarding the role of long fibre retention in the parietal pleura, inflammation and mesothelioma. Part. Fibre Toxicol. 7 (1), 1–17.

Downs, R.T., Palmer, D.C., 1994. The pressure behavior of alpha cristobalite. Am Mineral. 79, 9–14.

Evans, J.C., Evans, R.J., Holmes, A., Hounam, R.F., Jones, D.M., Morgan, A., Walsh, M., 1973. Studies on the deposition of inhaled fibrous material in the respiratory tract of the rat and its subsequent clearance using radioactive tracer techniques: 1. UICC crocidolite asbestos. Environ. Res. 6, 180–201.

Fahimizadeh, M., Wong, L.W., Baifa, Z., Sadjadi, S., Auckloo, S.A.B., Palaniand, Y.K., Pasbakhsh, P., Tan, J.B.L., Singh, R.K.R., Yuan, P., 2024. Halloysite clay nanotubes: innovative applications by smart systems. Appl. Clay Sci. 251, art. no. 107319.

Fakhrullina, G.I., Akhatova, F.S., Lvov, Y.M., Fakhrullin, R.F., 2015. Toxicity of halloysite clay nanotubes in vivo: a Caenorhabditis elegans study. Env. Sci.: Nano 2 (1), 54–59.

Gbondo, D., Zhao, Y., Pham, M., Rumchev, K., 2024. Trends in Exposure to Respirable Dust and Respirable Crystalline Silica among Lithium Mine Workers in Western Australia. Saf. Health Work 15 (4), 481–490.

Gray-Wannell, N., Cubillas, P., Aslam, Z., Holliman, P.J., Greenwell, H.C., Brydson, R., Delbos, E., Strachan, M.J., Fuller, M., Hillier, S., 2023. Morphological features of halloysite nanotubes as revealed by various microscopies. Clay Miner. 58 (4), 395–407.

Gualtieri, A.F., 2018. Towards a quantitative model to predict the toxicity/pathogenicity potential of mineral fibers. Toxicol. Appl. Pharmacol. 361, 89–98.

Gualtieri, A.F., 2021. Bridging the gap between toxicity and carcinogenicity of mineral fibres by connecting the fibre crystal-chemical and physical parameters to the key characteristics of cancer. Curr. Res. Toxicol. 2, 42–52.

Gualtieri, A.F., 2023. Journey to the Centre of the lung. The perspective of a mineralogist on the carcinogenic effects of mineral fibres in the lungs. J. Hazard. Mater. 442, 130077.

Gualtieri, A.F., Mossman, B.T., Roggli, V.L., 2017. Towards a general model for predicting the toxicity and pathogenicity of mineral fibres. Chapter 15. In: Gualtieri, A.F. (Ed.), Mineral Fibres: Crystal Chemistry, Chemical-Physical Properties, Biological Interaction and Toxicity, vol. 18. European Mineralogical Union - EMU Notes in Mineralogy, pp. 501–532.

Gualtieri, A.F., Pollastri, S., Bursi Gandolfi, N., Gualtieri, M.L., 2018. *In vitro* acellular dissolution of mineral fibres: a comparative study. Sci. Rep. 8 (1), 7071.

Gualtieri, A.F., Leoncini, M., Rinaldi, L., Zoboli, A., Di Giuseppe, D., 2021. WebFPTI: a tool to predict the toxicity/pathogenicity of mineral fibres including asbestos. Earth Sci. Inf. 14, 2401–2409.
Gualtieri, A.F., Cocchi, M., Muniz-Miranda, F., Pedone, A., Castellini, E., Strani, L., 2024. Iron nuclearity in mineral fibres: Unravelling the catalytic activity for predictive modelling of toxicity. J. Hazard. Mater. 469, 134004.
Gunter, M.E., 2018. Elongate mineral particles in the natural environment. Toxicol. Appl. Pharmacol. 361, 157–164.
Hart, R.D., Gilkes, R.J., Siradz, S., Singh, B., 2002. The nature of soil kaolins from Indonesia and Western Australia. Clay Clay Miner. 50, 198–207.
Huang, R., Wu, L., Wang, X., Tang, N., Gao, L., Wang, A., Lu, Y., 2024. Review on the effect of isomorphic replacement on the structure and application performance of typical clay minerals. Prog. Nat. Sci.: Mater. Int. 34 (2), 251–262.
IARC (International Agency for Research on Cancer), 2012. Silica Dust, Crystalline, in the Form of Quartz or Cristobalite. A Review of Human Carcinogens: Arsenic, Metals, Fibres and Dusts. International Agency for Research on Cancer, Lyon, France, pp. 356–405.
Jaurand, M.C., 2016. An overview on the safety of tubular clay minerals. Dev. Clay Sci. 7, 485–508.
Jones, R.M., Batteate, C., 2024. Preventing Silicosis: Meeting Report and Recommendations. Fielding School of Public Health, University of California, Los Angeles, Center for Occupational and Environmental Health, pp. 1–35.
Joussein, E., Petit, S., Churchman, J., Theng, B., Righi, D., Delvaux, B.J.C.M., 2005. Halloysite clay minerals—a review. Clay Miner. 40 (4), 383–426.
Keeling, J.L., Pasbakhsh, P., Churchman, G.J., 2015. The mineralogy, geology and occurrences of halloysite. Natural Mineral Nanotubes, Apple Academic Press, pp. 95–115.
Kihara, K., 1990. An X-ray study of the temperature dependence of the quartz structure – Eur. Aust. J. Mineral. 2, 63–77.
Koivisto, A.J., Bluhme, A.B., Kling, K.I., Fonseca, A.S., Redant, E., Andrade, F., Sørig Hougaard, K., Krepker, M., Setter Prinz, O., Segal, E., Holländer, A., Jensen, K.A., Vogel, U., Koponen, I.K., 2018. Occupational exposure during handling and loading of halloysite nanotubes–a case study of counting nanofibers. NanoImpact 10, 153–160.
Komusiński, J., Stoch, L., Dubiel, S.M., 1981. Application of Electron Paramagnetic Resonance and Mössbauer Spectroscopy in the Investigation of Kaolinite-Group Minerals. Clay Clay Miner. 29, 23–30.
Koppenol, W.H., Hider, R.H., 2019. Iron and redox cycling. Do'S Don'ts. Free Radic. Biol. Med. 133, 3–10.
Lampropoulou, P., Papoulis, D., 2021. Halloysite in Different Ceramic Products: a Review. Materials 14, 5501.
Lazzara, G., Cavallaro, G., Panchal, A., Fakhrullin, R., Stavitskaya, A., Vinokurov, V., Lvov, Y., 2018. An assembly of organic-inorganic composites using halloysite clay nanotubes. Curr. Opin. Colloid Interface Sci. 35, 42–50.
Lazzara, G., Bruno, F., Brancato, D., Sturiale, V., D'Amico, A.G., Miloto, S., Pasbakhsh, P., D'Agata, V., Saccone, S., Federico, C., 2023. Biocompatibility analysis of halloysite clay nanotubes. Mater. Lett. 336, 133852.
Leporatti, S., Cascione, M., De Matteis, V., Rinaldi, R., 2020. Design of nano-clays for drug delivery and bio-imaging: can toxicity be an issue? Nanomedicine 15 (25), 2429–2432.
Levis, S.R., Deasy, P.B., 2002. Characterisation of halloysite for use as a microtubular drug delivery system. Int. J. Pharm. 243 (1–2), 125–134.
Liu, H.Y., Du, L., Zhao, Y.T., Tian, W.Q., 2015. *In vitro* hemocompatibility and cytotoxicity evaluation of halloysite nanotubes for biomedical application. J. Nanomater. 2015 (1), 685323.
Long, Z., Wu, Y.P., Gao, H.Y., Zhang, J., Ou, X., He, R.R., Liu, M., 2018. *In vitro* and *in vivo* toxicity evaluation of halloysite nanotubes. J. Mater. Chem. B 6 (44), 7204–7216.
Luo, Y., Humayun, A., Murray, T.A., Kemp, B.S., McFarland, A., Liu, X., Mills, D.K., 2020. Cellular Analysis and Chemotherapeutic potential of a Bi-Functionalized Halloysite Nanotube. Pharmaceutics 12, 962.
Lynch, I., Dawson, K.A., 2008. Protein-nanoparticle interactions. Nano Today 3, 40–47.
Maisanaba, S., Pichardo, S., Puerto, M., Gutierrez-Praena, D., Camean, A.M., Jos, A., 2015. Toxicological evaluation of clay minerals and derived nanocomposites: a review. Environ. Res. 138, 233–254.
Massaro, M., Cavallaro, G., Colletti, G.C., D'Azzo, G., Guernelli, S., Lazzara, G., Pieraccini, S., Riela, S., 2018a. Halloysite nanotubes for efficient loading, stabilization and controlled release of insulin. J. Colloid Interface Sci. 524, 156–164.
Massaro, M., Campofelice, A., Colletti, C.G., Lazzara, G., Noto, R., Riela, S., 2018b. Functionalized halloysite nanotubes: efficient carrier systems for antifungine drugs. Appl. Clay Sci. 160, 186–192.
Molinari, C., Conte, S., Dondi, M., Zanelli, C., 2024. Content of crystalline silica phases in porcelain stoneware. Open Ceram. 19, 100650.
MSHA (Mine Safety and Health Administration), 2024. 28218 Department of Labor Federal Register / Vol. 89, No. 76 / Thursday, April 18, 2024 / Rules and Regulations.
Muller, J.P., Calas, G., 1989. Tracing kaolinites through their defect centres: Kaolinite paragenesis in a laterite (Cameroon). Econ. Geol. 84, 694–707.
Naumenko, E.A., Fakhrullin, R.F., 2017. Toxicological evaluation of clay nanomaterials and polymer–clay nanocomposites. In: Lvov, Y., Guo, B., Fakhrullin, R.F. (Eds.), Functional Polymer Composites with Nanoclays, pp. 399–419.
NIOSH, 2011. (National Institute for Occupational Safety and Health), Current Intelligence Bulletin 62. Asbestos Fibers and Other Elongate Mineral Particles: State of the Science and Roadmap for Research. Revised Edition. https://www.cdc.gov/niosh/docs/2011-159/pdfs/2011-159.pdf (Accessed January 03, 2025).
Pasbakhsh, P., Churchman, G.J., Keeling, J.L., 2013. Characterisation of properties of various halloysites relevant to their use as nanotubes and microfibre fillers. Appl. Clay Sci. 74, 47–57.
Pirngruber, G.D., Roy, P.K., Prins, R., 2006. On determining the nuclearity of iron sites in Fe-ZSM-5—a critical evaluation. Phys. Chem. Chem. Phys. 8 (34), 3939–3950.
Pochapski, D.J., Carvalho dos Santos, C., Leite, G.W., Pulcinelli, S.H., Santilli, C.V., 2021. Zeta potential and colloidal stability predictions for inorganic nanoparticle dispersions: Effects of experimental conditions and electrokinetic models on the interpretation of results. Langmuir 37 (45), 13379–13389.
Pollastri, S., Gualtieri, A.F., Gualtieri, M.L., Hanuskova, M., Cavallo, A., Gaudino, G., 2014. The zeta potential of mineral fibres. J. Hazard. Mater. 276, 469–479.
Rong, R., Zhang, Y., Zhang, Y., Hu, Y., Yang, W., Hu, X., Wen, L., Zhang, Q., 2019. Inhibition of inhaled halloysite nanotube toxicity by trehalose through enhanced autophagic clearance of p62. Nanotoxicology 13 (3), 354–368.
Rozhina, E., Batasheva, S., Miftakhova, R., Yan, X., Vikulina, A., Volodkin, D., Fakhrullin, R., 2021. Comparative cytotoxicity of kaolinite, halloysite, multiwalled carbon nanotubes and graphene oxide. Appl. Clay Sci. 205, 106041.
Sánchez-Fernández, A., Peña-Parás, L., Vidaltamayo, R., Cué-Sampedro, R., Mendoza-Martínez, A., Zomosa-Signoret, V.C., Rivas-Estilla, A.M., Riojas, P., 2014. Synthesization, characterization, and *in vitro* evaluation of cytotoxicity of biomaterials based on halloysite nanotubes. Materials 7 (12), 7770–7780.
Santos, A.C., Pereira, I., Reis, S., Veiga, F., Saleh, M., Lvov, Y., 2019. Biomedical potential of clay nanotube formulations and their toxicity assessment. Expert Opin. Drug Deliv. 16 (11), 1169–1182.
Sawicka, D., Zapor, L., Chojnacka-Puchta, L., Miranowicz-Dzierzawska, K., 2021. The *in vitro* toxicity evaluation of halloysite nanotubes (HNTs) in human lung cells. Toxicol. Res. 37 (3), 301–310.
Schroeder, P.A., Shiflet, J., 2000. Ti-bearing phases in the Huber Formation: an East Georgia kaolin deposit. Clay Clay Miner. 48, 151–158.
Smith, M.T., Guyton, K.Z., Gibbons, C.F., Fritz, J.M., Portier, C.J., Rusyn, I., DeMarini, D. M., Caldwell, J.C., Kavlock, R.J., Lambert, P.F., Hecht, S.S., Bucher, J.R., Stewart, B. W., Baan, R.A., Cogliano, V.J., Straif, K., 2016. Key characteristics of carcinogens as a basis for organizing data on mechanisms of carcinogenesis. Environ. Health Perspect. 124 (6), 713–721.
Soma, M., Churchman, G.J., Theng, B.K.G., 1992. X-ray photoelectron spectroscopic analysis of halloysites with different composition and particle morphology. Clay Miner. 27, 413–421.
Stanton, M.F., Layard, M., Tegeris, A., Miller, E., May, M., Morgan, E., et al., 1981. Relation of particle dimension to carcinogenicity in amphibole asbestoses and other fibrous minerals. J. Natl. Cancer Inst. 67, 965–975.
Steenland, K., Ward, E., 2014. Silica: a lung carcinogen. CA: a cancer journal for clin, 64 (1), 63–69.
SWA (Safe Work Australia) 2024. Working with crystalline silica substances Guidance for PCBUs, JULY 2024, pp. 84.
Tarasova, E., Naumenko, E., Rozhina, E., Akhatova, F., Fakhrullin, R., 2019. Cytocompatibility and uptake of polycations-modified halloysite clay nanotubes. Appl. Clay Sci. 169, 21–30.
Tóth, G., Hermann, T., Da Silva, M.R., Montanarella, L., 2016. Heavy metals in agricultural soils of the European Union with implications for food safety. Environ. Int. 88, 299–309.
van Oss, C.J., Naim, J.O., Costanzo, P.M., Giese, R.F., Wu, W., Sorling, A.F., 1999. Impact of different asbestos species and other mineral particles on pulmonary pathogenesis. Clay Clay Miner. 47, 697–707.
Vergaro, V., Abdullayev, E., Lvov, Y.M., Zeitoun, A., Cingolani, R., Rinaldi, R., Leporatti, S., 2010. Cytocompatibility and uptake of halloysite clay nanotubes. Biomacromolecules 11 (3), 820–826.
Wang, X., Gong, J., Rong, R., Gui, Z., Hu, T., Xu, X., 2018. Halloysite nanotubes-induced Al accumulation and fibrotic response in lung of mice after 30-day repeated oral administration. J. Agric. Food Chem. 66 (11), 2925–2933.
Watanabe, Y., Kitagawa, Y., Sugo, S., 1969. Structural aspects of clay minerals occurring in some soils. In: Heller, L. (Ed.), Proceedings of the International Clay Conference 1969. Israel University Press, Tokyo, pp. 129–140.
Wei, W., Minullina, R., Abdullayev, E., Fakhrullin, R., Mills, D., Lvov, Y., 2014. Enhanced efficiency of antiseptics with sustained release from clay nanotubes. RSC Adv. 4, 488–494.
Wilson, I.R., 2004. Kaolin and halloysite deposits of China. Clay Miner. 39, 1–15.
Wilson, I.R., Keeling, J., 2016. Global occurrence, geology and characteristics of tubular halloysite deposits. Clay Miner. 51 (3), 309–324.
Wu, B., Jiang, M., Liu, X., Huang, C., Gu, Z., Cao, Y., 2020. Evaluation of toxicity of halloysite nanotubes and multi-walled carbon nanotubes to endothelial cells *in vitro* and blood vessels in vivo. Nanotoxicology 14 (8), 1017–1038.
Wylie, A.G., Korchevskiy, A.A., Van Orden, D.R., Chatfield, E.J., 2022. Discriminant analysis of asbestiform and non-asbestiform amphibole particles and its implications for toxicological studies. Comput. Toxicol. 23, 100233–100249.
Yang, L., Steefel, C.I., 2008. Kaolinite dissolution and precipitation kinetics at 22 C and pH 4. Geochim. Cosmochim. Acta 72 (1), 99–116.
Zecchina, A., Rivallan, M., Berlier, G., Lamberti, C., Ricchiardi, G., 2007. Structure and nuclearity of active sites in Fe-zeolites: comparison with iron sites in enzymes and homogeneous catalysts. Phys. Chem. Chem. Phys. 9, 3483–3499.
Zhang, J., Huang, Z., Yang, M., Dong, S., Zhou, F., Yan, C., Hu, Y., Yang, H., Gao, Y., 2025. Halloysite nanotubes potentiate protein assembly for facile fabrication of nanocomposite thin film and its application in wound dressing. Appl. Clay Sci. 272, 107816.
Zhao, X., Wan, Q., Fu, X., Meng, X., Ou, X., Zhong, R., Zhou, Q., Liu, M., 2019. Toxicity evaluation of one-dimensional nanoparticles using caenorhabditis elegans: a comparative study of halloysite nanotubes and chitin nanocrystals. ACS Sustain. Chem. Eng. 7 (23), 18965–18975.